

Investigation into non-equilibrium heat flow over patterned interfaces of battery electrodes.

Harry Mclean, MPhys

November 12, 2024

Abstract

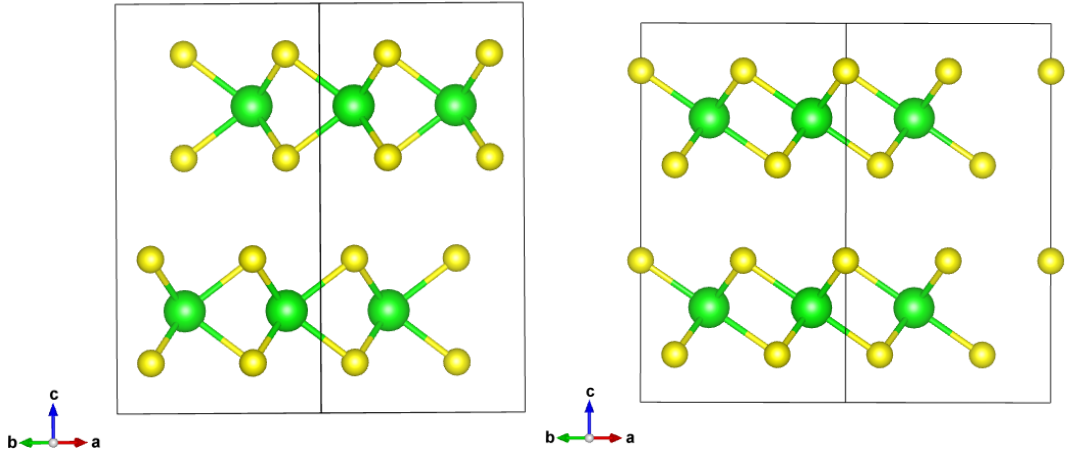
The objective of this project is to develop a multi-scale theoretical model of thermal transport that addresses the limitations of the Fourier model outside of equilibrium and create a new computational model to examine time-dependent heat flow in electrodes. Despite the critical role of thermal properties in battery performance, especially under non-equilibrium conditions, detailed theoretical models addressing these aspects are lacking. This study aims to fill this gap. This study uses Density Functional Theory (DFT) to analyze the thermal properties of Transition Metal Dichalcogenides (TMDCs) during ion intercalation and deintercalation. Additionally, we explore how electrode geometry affects thermal management within batteries, influencing heat dissipation and distribution. By identifying strategies to improve battery safety and longevity, this research aims to advance battery technology.

1 Introduction

1.1 Batteries

Rechargeable electrical batteries are used in many everyday portable electronics [1]. They are also used to increase the viability of renewable energy sources, which is a vital part of the future of climate management and sustainability [2]. However, their adoption has been slow with electric vehicles [3]. In the case of electric vehicles, capacity, stability, and increasing the rate at which the battery charges will significantly affect their adoption [4]. One of the contributing factors to the rate at which a battery can be charged is the higher temperatures that are achieved from the higher electrical currents needed for faster charging [5], this is an issue of thermal management.

An electrical battery is a device that stores electrical energy in bonds. The stored energy is released when atoms donate electrons and the resultant ions move across a potential difference gradient to a lower energy state. Energy has been released in this process in the form of electrical current. In a rechargeable battery, the electrode's host structure (the material that is not transported across the electrolyte) has been reversibly altered. Conversion



(a) A 2x2x1 supercell H phase of Zirconium disulphide
(b) A 2x2x1 supercell T phase of Zirconium disulphide

Figure 1: Figures 1a & 1b shows a representation of the TMDC layered atomic structure of Zirconium disulphide, green is Zirconium, yellow is Sulphur.

and intercalation are the two typical reversible processes involving strong (ionic or covalent) and weak (typically Van Der Waals) bond interactions respectively. In conversion batteries, the host electrode is structurally transformed into new compounds destroying its original structure (i.e. $\text{ZrS}_2 + 4\text{Li} \rightarrow 2\text{Li}_2\text{S} + \text{Zr}$ [6]). In intercalation batteries, the host material accepts the ion in the vacant sites in its structure (i.e. $\text{ZrS}_2 + \text{Li} \rightarrow \text{LiZrS}_2$ [6]). Fig. 1 shows the typical layered structure. The ions can move back across the electrolyte (not electrons) and store energy by applying a potential difference gradient in the opposite direction. The structure of a typical battery is shown in Fig. 2.

The process of charging and discharging is not efficient. Energy is lost through heat and in phase changes of the material. The principle heat carriers and the mechanism behind the phase transitions (changes in the structure of a crystal lattice) are related to the behaviour of phonons (a quantised excitation of a crystal lattice) [8, 9].

Thermal management is an important factor in batteries [10] as stated above, increasing temperature generally leads to greater energy loss and faster battery ageing [5]. In batteries, this increase in temperature can lead to phase changes in the electrodes that reduce cyclability and energy storage. In extreme cases, this can cause the battery to ignite and explode [11].

This report is based on the hypothesis that the change in thermal conductivity dramatically affects battery thermal management. Understanding this leads to a longer battery lifetime, higher charging efficiency, and faster charging capabilities.

Cahill *et al.* showed that the thermal conductivity changes an order of magnitude during charging. This study measured the effect of lithium concentration on the thermal conductivity

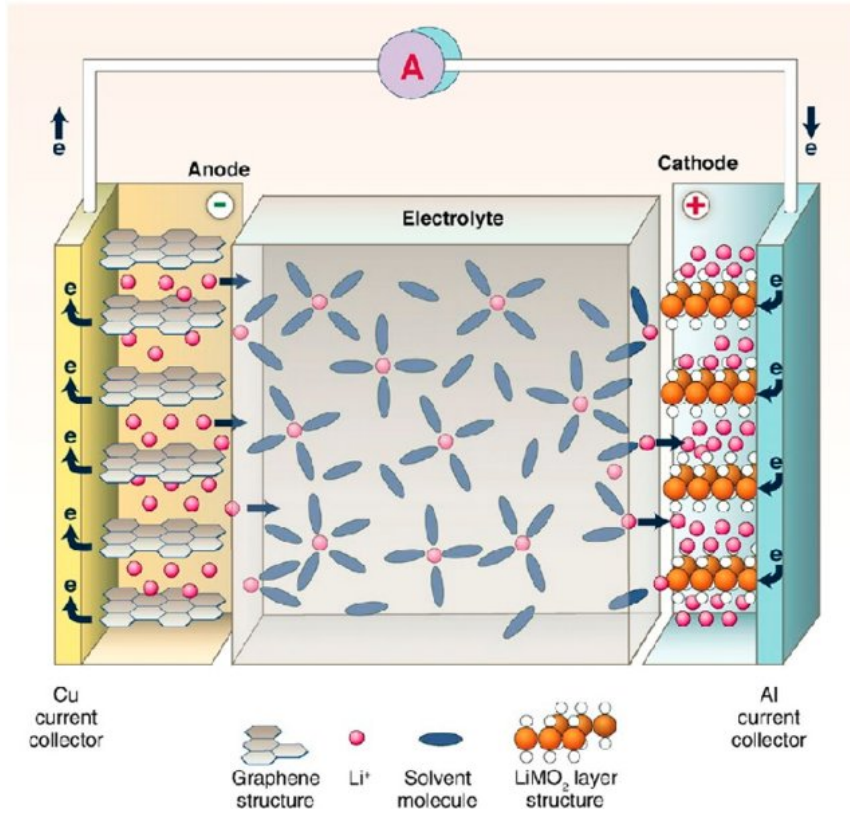


Figure 2: A simple schematic of a lithium-ion battery [7], assuming a generic metal oxide cathode, a liquid electrolyte, and a hard carbon anode. The figure shows the discharging cycle of a battery.

of MoS₂ through the plane and in the plane [12]. They showed a significant drop (\approx one order of magnitude) and a subsequent increase in the thermal conductivity between $x = 0.2$ and $x = 0.5$, shown in Fig. 3. The study also showed how the thermal conductivity is directional (through and in-plane differences). Many batteries are made from Transition Metal Dichalcogenides (TMDCs) [14]. These are layered materials consisting of transition metals and chalcogen (i.e. Sulphur(s), Selenium (Se) and Tellurium (Te)). Early success with these has been demonstrated by TiS₂ the first reversible lithium ion electrode [6, 15]. Due to the layered nature of TMDCs, they have the potential to achieve high amounts of lithium intercalation into the gaps between the layers (see Fig. 1). There have been extensive studies on ion intercalation into a wide range of TMDCs [16, 17, 18].

Although current industry standards are oxide materials, many experimental and theoretical investigations have been conducted scowering all material types for a better alternative (intercalation examples include metal oxides, NMC, NMA, TMDCs, and MXenes [19, 20]). The TMDC ZrS₂ holds promise for use as an electrode material. ZrS₂ exhibits reversible chemical conversion (i.e $ZrS_2 + 4Li \rightarrow 2Li_2S + Zr$) at low operating voltages, 0.3V, just like TiS₂. The ZrS₂ experimentally investigated chemical conversion [6] can lead to higher energy densities as more lithium can be stored compared to the intercalation. The downside

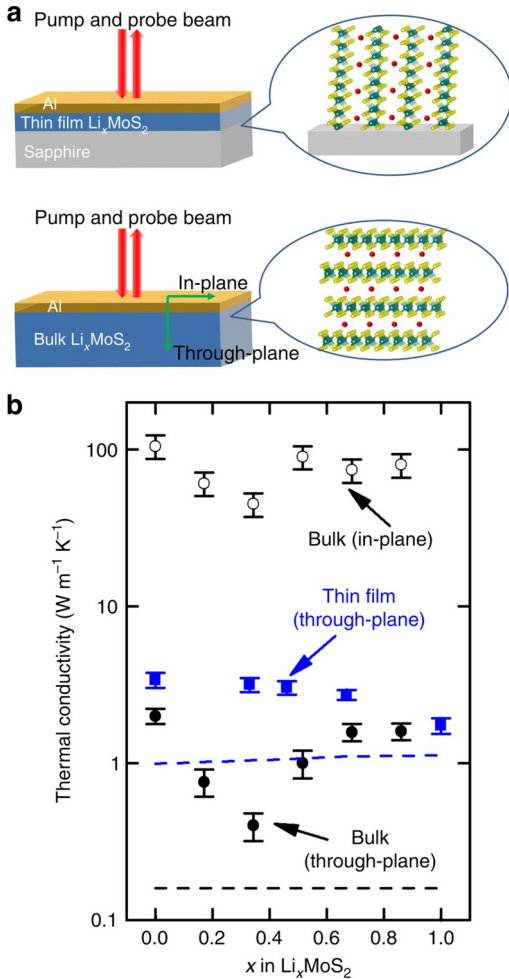


Figure 3: Experimental measurement of the through an in-plane thermal conductivity of MoS_2 at different amounts of Li intercalation [12]. a) Schematics for measuring thermal conductivity using TDTR (Time-domain thermoreflectance [13]). b) Results of the experimental investigation. Figure taken from [12]

is this occurs at low operating voltages. While low operating voltages present a problem the elementary components of elementary components of ZrS_2 are relatively abundant in the Earth crust [21] compared to the Cobalt, Nickle, and Magnesium used in electrodes in current industry standard [14].

ZrS_2 shows experimental capacities between 300-500 mAh/g [6] for lithium intercalation with theoretically achievable values of 700 mAh/g, [16, 22]. The energy density of ZrS_2 is significantly above the industry standard of $\approx 200 \text{ mAh/g}$ [23]. In addition, ZrS_2 shows in theoretical investigations signs of high energy density for magnesium ion intercalation [16], and magnesium has a much higher abundance in the Earth crust than lithium [21]. These properties make it favourable to investigation due to the promise of a sustainable and mass-producible battery.

The phase changes and the thermal stability of ZrS_2 remain unexplored. Nor are the directionality and variation in lattice thermal conductivity. These factors will have a significant effect on the macroscopic thermal properties of the electrode. By understanding ZrS_2 we can hope to understand all TMDCs in principle.

Modelling thermal transport is challenging, as is calculating the thermal properties. Heat transport theory is unfinished. Its foundation lies in Fourier's heat equation,

$$\dot{Q} = -\kappa A \frac{\Delta T}{\Delta L}, \quad (1)$$

where \dot{Q} is the heat flux, κ is thermal conductivity, A is area, T is temperature and L is distance. The Fourier heat equation doesn't constrain the time for energy to diffuse throughout the system. This is a clear violation of special relativity [24], and results in instantaneous thermal transport.

Normally the shortcomings of Fourier are not an issue. However, in investigations with dynamic effects (such as in batteries with temporal and spatial dynamics), this should be considered. This has to be tackled at two levels the macroscopic and the atomic.

2 Macroscale (Thermal modelling)

2.1 Fourier

Fourier proposed the first form of heat conduction

$$\frac{dQ}{dt} = -\kappa A \frac{\Delta T}{\Delta x} \quad (2)$$

where Q is the amount of heat energy, T is temperature, κ is the thermal conductivity, A is the Area and x and t are length and time respectively. Note this is derived using the assumption

that the distribution is in equilibrium [25]. This equation has formed the foundation for macro-scale heat transport.

The classical derivation is as follows. Using the thermal flux, Fourier's thermal transport equation can be derived from the continuity equation,

$$\int J \cdot da = \frac{dQ}{dt} \quad (3)$$

where J is the thermal heat flux and Q is the thermal energy. The continuity equation (equation 3) is transformed into,

$$\int (\nabla \cdot J dV) = \frac{dQ}{dt} \quad (4)$$

via the divergence theorem. The total thermal energy in the system in terms of the heat capacity is,

$$Q = \int \rho C_V (T - T_0) dV = \int \rho C_V \Delta T dV, \quad (5)$$

it can also be expressed as

$$\frac{dQ}{dt} = \int \rho C_V \frac{dT}{dt} dV. \quad (6)$$

Using equation 6 and 3,

$$\int (\nabla \cdot J dV) = \int \rho C_V \frac{dT}{dt} dV. \quad (7)$$

Using equation 7 and thermal heat flux defined as,

$$J = -\kappa \nabla T, \quad (8)$$

using Eq. 2 the Fourier heat equation takes the familiar first-order form of,

$$\rho C_V \frac{dT}{dt} = \nabla \cdot (\kappa \nabla T). \quad (9)$$

The main issue with Fourier's law as previously stated is, no matter how long the system has been outside of the steady state ($\frac{dT}{dt} \neq 0$) there will be a change in temperature at all points in space as shown in Fig. 4.

2.2 Cattaneo

The shortcomings of Fourier can be resolved by adding a correction, that introduces a finite propagation speed to the flow of heat. Cattaneo [26], and others [27] have discussed this. It usually takes the form

$$\tau \rho C_V \frac{d^2 T}{dt^2} + \rho C_V \frac{dT}{dt} - P = \nabla \cdot (\kappa \nabla T) \quad (10)$$

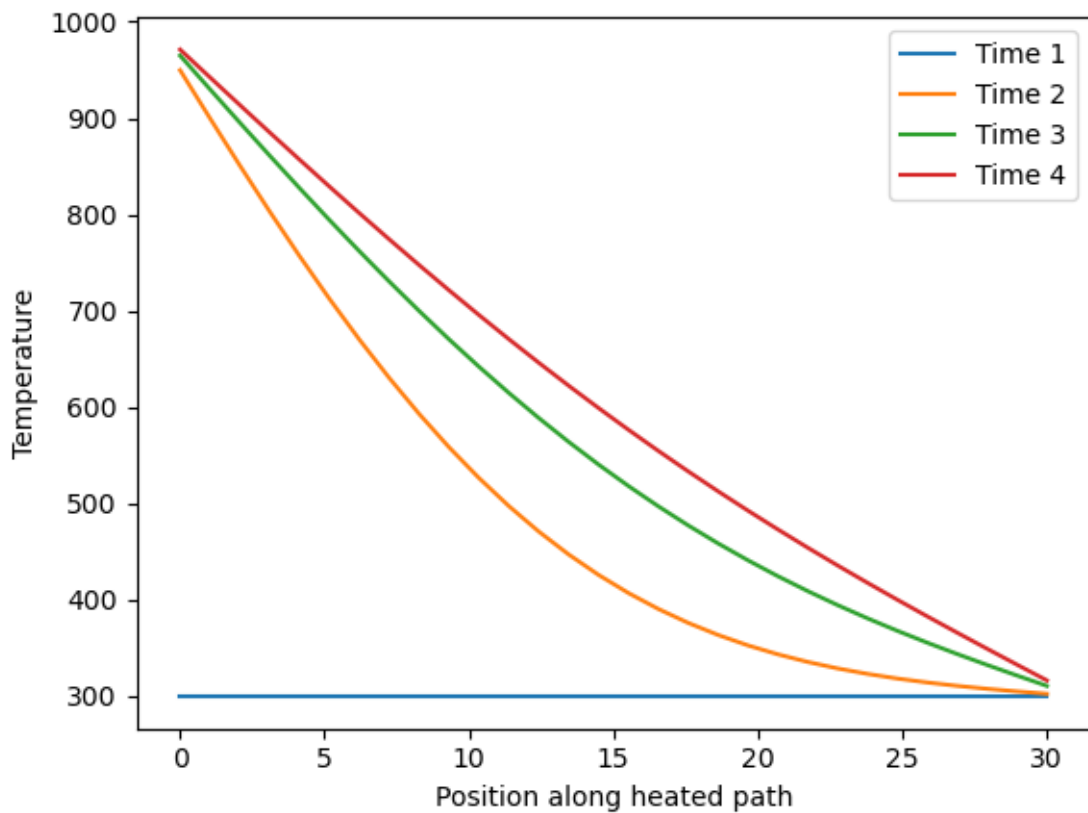


Figure 4: A graph of a 1D system with a fixed hot bath of 1000K on the left and a fixed sink at the right at 300K. The graph shows, in the Fourier model, that for each increase in time, there is a change in temperature at every position from the previous time.

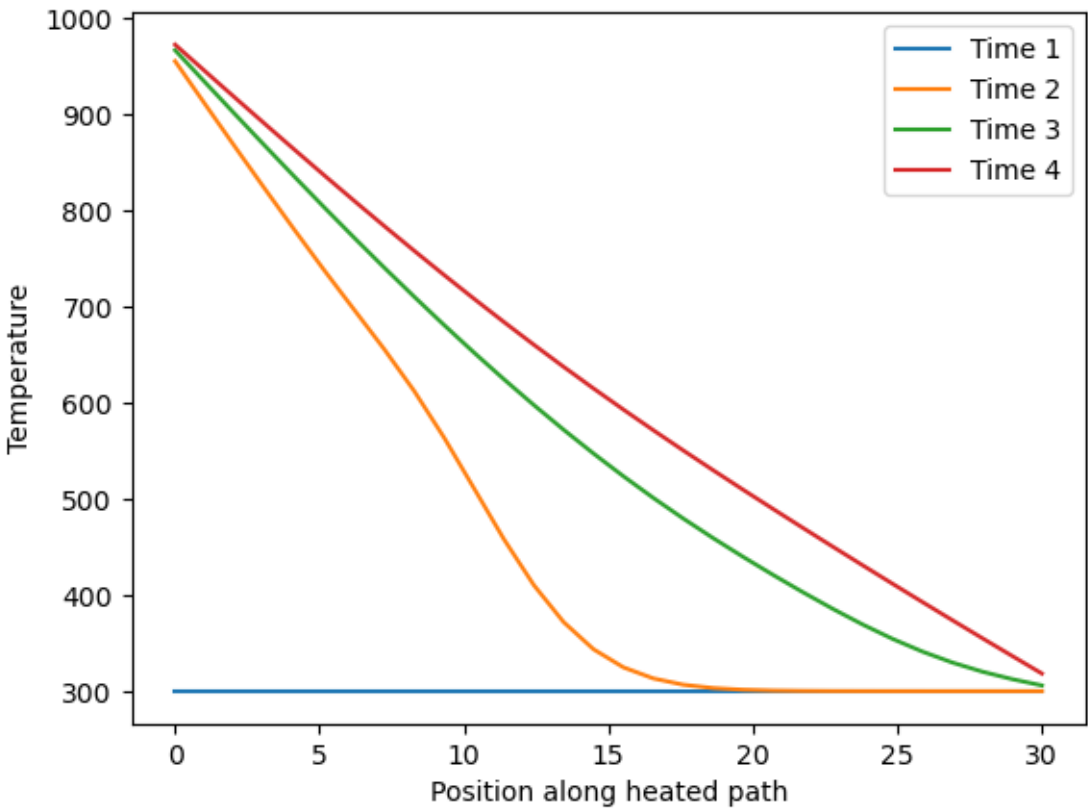


Figure 5: Graph representing Cattaneo heat flow for the same system shown in the Fourier case in Fig. 4. Not all positions along the same system have a temperature change, there is a limit to how fast the heat can travel.

Here T is the temperature, t is the time, τ is the Cattaneo correction, P is the power density (power per unit volume), ρ is the mass density and C_V is the heat capacity at a constant volume, and κ is the thermal conductivity.

The Cattaneo correction to Fourier introduces a wave propagation term analogous to the Telegraphers equation (see Appendix A)[28]. The result is best demonstrated with the comparison of Fig. 5 and Fig. 4. It can be seen there is a limit to how fast the heat can travel.

The challenge with Cattaneo heat flow is the solution to the equation can take the form of a hyperbolic equation (Fourier is parabolic)[29]. This means the system becomes difficult to solve analytically with temporal and spatial variances. Secondly, the τ term is ill-defined, and thus one requirement is an effective design for measurement validating Cattaneo.

Part of the project involves investigating the τ terms effect on complex nano and macroscopic scale systems to design an experiment to validate its existence. For example, such systems could be the system's response to high-frequency power such as transistors in processors, thermoacoustic systems, and systems with non-uniform thermal conductivity (ion interca-

lated electrodes creating regions of varying τ).

2.3 Derivation from Boltzmann transport equation

Cattaneo's correction comes from an empirical observation [26], here I propose a new derivation from first principles. Start with the following derivation of the continuity equation using the Boltzmann transport equation. The classic approach is that the distribution function can be written as a function in terms of momentum, position and time,

$$f = f(\text{momentum} = \rho, \text{position} = r, \text{time} = t). \quad (11)$$

The distribution function, expressed in terms of momentum, position, and time, is expanded using partial derivatives,

$$\frac{df}{dt} = \frac{\delta f}{\delta \rho} \cdot \frac{\delta \rho}{\delta t} + \frac{\delta f}{\delta r} \cdot \frac{\delta r}{\delta t} + \frac{\delta f}{\delta t}. \quad (12)$$

Then, convert partials to some standard terms,

$$\frac{df}{dt} = \frac{\delta f}{\delta \rho} \cdot F + \frac{\delta f}{\delta r} \cdot v + \frac{\delta f}{\delta t}. \quad (13)$$

The force, F , is typically said to be 0 as it represents an external force acting on the distribution.

We now define the internal energy density and heat flux in terms of the sum of all phonon modes (q_s) of the phonon frequency (ω_{qs}) and velocity (v_{qs}),

$$U = \frac{1}{V} \sum_{qs} \hbar \omega_{qs} f_{qs} \quad (14)$$

$$J = \frac{1}{V} \sum_{qs} \hbar \omega_{qs} v_{qs} f_{qs} \quad (15)$$

We multiply Eq. 13 through by $\hbar \omega_{qs}$ (also assuming $v = v_{qs}$). We then substitute Eq. 14 & 15 into 12, and then using the assumption that the $\frac{dU}{dt} = P$, where P is a power density to obtain,

$$P = \nabla \cdot J + \frac{\delta U}{\delta t}. \quad (16)$$

This is the continuity equation where U is the internal energy density, J is the heat flux, and P is the power density.

To derive Cattaneo we start with the steady-state definition of thermal conductivity as defined by Fourier,

$$J_{\text{steady}} = -\kappa \nabla T. \quad (17)$$

The internal energy density can also be stated as,

$$\delta U = \rho C_v \delta T, \quad (18)$$

where ρ is density, and C_v is the specific heat capacity at constant volume. Here we state that,

$$f_\lambda = \bar{f}_\lambda + s_\lambda \quad (19)$$

where s is some small shift from equilibrium, and λ represents a single state. We also state,

$$\dot{f}_\lambda = -\frac{f_\lambda - \bar{f}_\lambda}{\tau} = -\frac{s_\lambda}{\tau} \quad (20)$$

where τ is the average relaxation time (this is the same reasoning for its use in the linearised Boltzmann method [25]). Then the distribution becomes,

$$f_\lambda = \bar{f}_\lambda - \tau \dot{f}_\lambda. \quad (21)$$

Knowing heat flux has the form Eq. 15 and multiplying through by $\frac{1}{V}, \hbar\omega_\lambda$, and v_λ , then summing over all states (λ) the resulting equation,

$$J = q_{\text{steady}} - \tau \dot{J}, \quad (22)$$

is the Cattaneo equation (also using Eq. 17),

$$J + \tau \dot{J} = -\kappa \nabla T. \quad (23)$$

Using Eq. 16, and assuming power is zero. Taking the divergence of the heat flux equation,

$$\tau \frac{d(\nabla \cdot J)}{dt} + \nabla \cdot J = -\nabla \cdot (\kappa \nabla T). \quad (24)$$

Then rearrange Eq. 16 for $\nabla \cdot J$ and substitute into the above. Then with the use of Eq. 18 we finally arrive at the Cattaneo heat flow equation,

$$\nabla \cdot (\kappa \nabla T) = \rho C_V \frac{\delta T}{\delta t} + \tau \rho C_V \frac{\delta^2 T}{\delta t^2}. \quad (25)$$

We note if thermal conductivity is isotropic in space we can replace this with the thermal diffusivity defined as,

$$\alpha = \frac{\kappa}{\rho C_V}. \quad (26)$$

We can restate Eq. 25,

$$\frac{\alpha}{\tau} (\nabla^2 T) = \frac{1}{\tau} \frac{\delta T}{\delta t} + \frac{\delta^2 T}{\delta t^2}. \quad (27)$$

where $\alpha/\tau \approx v^2$.

2.4 Additional power term

Assuming a time-dependent power input, we modify the heat flow equation to include an oscillatory heating component, enhancing symmetry between stored and added energy. This modification can be systematically derived by starting from the continuity equation with the additional power term and proceeding through the substitution of the heat flux term. This approach leads to a heat flow equation that accounts for time-dependent power contributions.

Using, Eq. 16, with non-zero power (P) into Eq. 23 via the steps previously mentioned we obtain,

$$\rho C_V \frac{dT}{dt} + \tau \rho C_V \frac{d^2T}{dt^2} - (P + \tau \frac{dP}{dt}) = \nabla \cdot (\kappa \nabla T) \quad (28)$$

This is the standard heat flow equation with an additional power time dependence.

2.5 Method

The finite element method for solving partial differential equations is commonly used in computational models, such as COMSOL. Finite element methods may produce unphysical results, such as negative temperature regions adjacent to high-temperature areas, this is a result of using smoothing functions. This has been observed in Comsol simulations where a heat pulse would result in negative temperature regions next to an area of much higher temperature [30]. This has not been observed to the author's knowledge experimentally so a different method for simulation heat flow has been considered, the implicit finite difference method. In the implicit method, the spatial components of a system are a function of itself. In the explicit method, the spacial components are only a function of the adjacent space. The explicit finite difference method has been found to run into significant issues with generating negative temperatures depending on the time evolution size and grid size [31], which is also an issue in the finite element method. Similarly, the explicit method doesn't simulate the steady state particularly well, due to the need to solve each cell iteratively.

Simulation of Fourier and Cattaneo

To solve Eq. 25 we have developed an implicit finite difference simulation, here I refer to this package as Heat Flow.

In Heat Flow, Eq. 25 is transformed into the form,

$$H_{IJ} T_J = S_J, \quad (29)$$

where H_{IJ} is the heat flow matrix, T_J is the temperature vector containing the temperatures of the system in its current state, and

$$S_J = \frac{-T_{PP,J}}{(2\delta t)}(\rho_i c_i) - [B_J + P_J + S_{cat}]. \quad (30)$$

Here, S_J consists of the previous previous time evolution temperatures $T_{PP,J}$ (originating from the central difference method), the boundary terms B_J and the Cattaneo correction S_{cat} . To derive the above (Eq. 29) we follow the following derivation: We start by rewriting 25 as,

$$\frac{dT}{dt} \rho C_V - P + (\rho C_V) \tau \frac{d^2T}{dt^2} = H(\kappa, \mathbf{r}) T. \quad (31)$$

Then, replace the terms with their vector equivalents, and expand dT/dt and d^2T/dt^2 with the central difference expansions,

$$\frac{T_J - T_{J,PP}}{(2\delta t)}(\rho C_V) - P_J + \rho_J C_{VJ} \tau \frac{T_J - 2T_{J,P} + T_{J,PP}}{(\delta t)^2} = H(\kappa, \mathbf{r})T. \quad (32)$$

Collect the like terms of Temperature together,

$$T_i \left(\frac{\rho_J C_{VJ}}{(2\delta t)} + \rho_J C_{VJ} \frac{\tau}{(\delta t)^2} \right) - \frac{\rho_J C_{VJ}}{2\delta t} T_{J,PP} - P_J + S_{cat} = H(\kappa, \mathbf{r})T. \quad (33)$$

This is not the final form of the S_J and T_J of Eq. 29, to achieve the final result we must next consider the following derivation of the H_{IJ} matrix.

H-matrix

The H-matrix has two terms

$$H_{IJ} = H_{0,IJ} + H_{p,IJ} \quad (34)$$

where H_0 is the pure H-matrix and H_p is the periodic correction.

Using the implicit finite difference method, the H-matrix is expressed as,

$$\begin{aligned} H(\kappa, \mathbf{r})T &= \frac{1}{(\delta x)^2} \\ &[\left(\frac{2\kappa_{ix+1,iy,iz} \kappa_{ix,iy,iz}}{\kappa_{ix+1,iy,iz} + \kappa_{ix,iy,iz}} \right) (T_{ix+1,iy,iz} - T_{ix,iy,iz}) \\ &- \left(\frac{2\kappa_{ix-1,iy,iz} \kappa_{ix,iy,iz}}{\kappa_{ix-1,iy,iz} + \kappa_{ix,iy,iz}} \right) (T_{ix,iy,iz} - T_{ix-1,iy,iz}) \\ &+ \left(\frac{2\kappa_{ix,iy+1,iz} \kappa_{ix,iy,iz}}{\kappa_{ix,iy+1,iz} + \kappa_{ix,iy,iz}} \right) (T_{ix,iy+1,iz} - T_{ix,iy,iz}) \\ &- \left(\frac{2\kappa_{ix,iy-1,iz} \kappa_{ix,iy,iz}}{\kappa_{ix,iy-1,iz} + \kappa_{ix,iy,iz}} \right) (T_{ix,iy,iz} - T_{ix,iy-1,iz}) \\ &+ \left(\frac{2\kappa_{ix,iy,iz+1} \kappa_{ix,iy,iz}}{\kappa_{ix,iy,iz+1} + \kappa_{ix,iy,iz}} \right) (T_{ix,iy,iz+1} - T_{ix,iy,iz}) \\ &- \left(\frac{2\kappa_{ix,iy,iz-1} \kappa_{ix,iy,iz}}{\kappa_{ix,iy,iz-1} + \kappa_{ix,iy,iz}} \right) (T_{ix,iy,iz} - T_{ix,iy,iz-1})], \end{aligned} \quad (35)$$

when treating all directions as the same ($\delta x = \delta y = \delta z$). Eq. 35 can be compressed down by expressing κ coefficients using the notation of,

$$\kappa_{+x} = \frac{2\kappa_{ix+1,iy,iz} \kappa_{ix,iy,iz}}{\kappa_{ix+1,iy,iz} + \kappa_{ix,iy,iz}}, \quad (36)$$

and

$$\kappa_{-x} = \frac{2\kappa_{ix-1,iy,iz} \kappa_{ix,iy,iz}}{\kappa_{ix-1,iy,iz} + \kappa_{ix,iy,iz}} \quad (37)$$

with the same for the y and z directions, see "κ at cell boundaries" for the derivation of κ . The H matrix (Eq. 35) can add and absorb the additional terms from Eq. 33 collecting all

temperatures of the same evolution (T_J) transforming Eq. 35 into,

$$\begin{aligned}
H(\kappa, \mathbf{r})T = & \frac{1}{(\delta x)^2} \\
& [\kappa_{+x}(T_{ix+1, iy, iz} - T_{ix, iy, iz}) \\
& - \kappa_{-x}(T_{ix, iy, iz} - T_{ix-1, iy, iz}) \\
& + \kappa_{+y}(T_{ix, iy+1, iz} - T_{ix, iy, iz}) \\
& - \kappa_{-y}(T_{ix, iy, iz} - T_{ix, iy-1, iz}) \\
& + \kappa_{+z}(T_{ix, iy, iz+1} - T_{ix, iy, iz}) \\
& - \kappa_{-z}(T_{ix, iy, iz} - T_{ix, iy, iz-1})] \\
& - T_{ix, iy, iz} \left(\frac{\rho_{ix, iy, iz} C_{Vix, iy, iz}}{(2\delta t)} + \frac{\tau \rho_{ix, iy, iz} C_{Vix, iy, iz} \tau}{(\delta t)^2} \right)
\end{aligned} \tag{38}$$

which is the form of the H-matrix. Using the notation $(ix, iy, iz) \equiv J$, where J ranges from 1 and $nx \cdot ny \cdot nz$, we can re-express the 3D temperature vector (real space temperature distribution) as a single 1D vector (abstract 1D system representing real space) Eq. 39 ($J_{0,0,0} = 0$).

$$J_{ix, iy, iz} = \sum_{iz=1}^{nz} \sum_{iy=1}^{ny} \sum_{ix=1}^{nx} (J_{ix-1, iy-1, iz-1} + 1) \tag{39}$$

Hence, the H-matrix can finally be conveniently expressed in the form of a sparse diagonal matrix in the following way. First the central diagonal ($I = J$),

$$\begin{aligned}
H_{[(ix, iy, iz), (ix', iy', iz'), 0]} = & \\
H_{IJ, 0} = & - \\
& [(\kappa_{+x} + \kappa_{-x}) \\
& + (\kappa_{+y} + \kappa_{-y}) \\
& + (\kappa_{+z} + \kappa_{-z})] \\
& + \left(\frac{\rho_{ix, iy, iz} C_{Vix, iy, iz}}{(2\delta t)} + \frac{\tau \rho_{ix, iy, iz} C_{Vix, iy, iz} \tau}{(\delta t)^2} \right) = \kappa
\end{aligned} \tag{40}$$

and the off-diagonal term, where $I \neq J$. Here there is only one example, but it is cycled over all other cell boundary interactions.

$$\begin{aligned}
H_{[(ix+1, iy, iz), (ix, iy, iz), 0]} = & \\
H_{IJ, 0} = & \kappa_{+x}
\end{aligned} \tag{41}$$

and

$$\begin{aligned}
H_{[(ix-1, iy, iz), (ix, iy, iz), 0]} = & \\
H_{IJ, 0} = & \kappa_{-x}
\end{aligned} \tag{42}$$

with similar terms present for the y and z-axis, which result in 6 diagonal terms.

S-vector

The Heat Flow has all the terms which are linear included in the "S" vector, shown in Eq. 30. It is broken into easy-to-understand components that can be coded using a modular approach, the boundary vector \mathbf{B} , the power vector \mathbf{P} , the temperature evolution vector $\frac{1}{\delta t} \mathbf{T}_p$, and the Cattaneo correction \mathbf{S}_{cat} . As in the H-matrix, the contracted notation for (ix, iy, iz) is J . Where J is the index that loops over all cells in the system.

Temperature evolution vector

This is the easiest term to implement, arising from $\frac{dT}{dt}$. The time evolution is approximated with,

$$\frac{dT}{dt} \approx \frac{T_J - T_{J,PP}}{2\delta t} \quad (43)$$

where $T_{J,PP}$ is the temperatures stored for each element J in the previous previous time step (Following central difference first derivative) and (δt) is our time step size. Moving the unknown temperature to the right had side ($T_J = T_{ix,iy,iz}$) the temperature evolution vector becomes proportional too,

$$-\frac{T_{J,pp}}{2\delta t}. \quad (44)$$

Power vector

The power vector represents input energy from an external source at a particular cell J ,

$$P_J = \frac{\text{POWER}_{\text{of heated cell}}}{\text{Volume}_{\text{of heated cell}}}. \quad (45)$$

Cattaneo correction

The Cattaneo correction,

$$\frac{d^2T}{dt^2} \tau \rho C_V \quad (46)$$

can be expanded using the finite difference method

$$\frac{d^2T}{dt^2} = \frac{T_J - 2T_{J,P} + T_{J,PP}}{(\delta t)^2} \quad (47)$$

moving the unknown temperature $T_J = T_{ix,iy,iz}$ to the RHS leaving:

$$S_{cat} = \tau \rho C_V \frac{T_{J,PP} - 2T_{J,P}}{(\delta t)^2} \quad (48)$$

where τ is the single-mode phonon relaxation time.

Boundary vector

Our 3D system comprises $NX \times NY \times NZ$ cubes. To start, the boundary interaction between the system and the temperature bath is found in the diagonal (self-term) of the h-matrix. The boundary interactions are not represented as off-diagonal terms in the H matrix as they are not included in the temperature vector T .

$$\begin{aligned}
H(\kappa, \mathbf{r})T = & \frac{1}{(\delta x)^2} \\
& [(\kappa_{+x})(T_{ix+1,iy,iz} - T_{ix,iy,iz}) \\
& - (\kappa_{-x})(T_{ix,iy,iz} - T_{ix-1,iy,iz}) \\
& + (\kappa_{+y})(T_{ix,iy+1,iz} - T_{ix,iy,iz}) \\
& - (\kappa_{-y})(T_{ix,iy,iz} - T_{ix,iy-1,iz}) \\
& + (\kappa_{+z})(T_{ix,iy,iz+1} - T_{ix,iy,iz}) \\
& - (\kappa_{-z})(T_{ix,iy,iz} - T_{ix,iy,iz-1})] \\
& - T_{ix,iy,iz}\rho_{ix,iy,iz}C_{Vix,iy,iz} \left(\frac{1}{(2\delta t)} + \frac{\tau}{(\delta t)^2} \right)
\end{aligned} \tag{49}$$

But take $ix = 1$ for a cell at the boundary (κ_{+x} is the κ average of cell $x = 1$ and $x = 2$). The same method can be applied to the other terms, $iy = iz = 1$ but these all have the same result. Similarly, $ix = NX$ results in a similar result but for the other boundaries in our cell. So let's reexamine the previous equation. Here we assume the bath at the boundary is of the same length as the system cells,

$$\begin{aligned}
H(\kappa, \mathbf{r})T = & \frac{1}{(\delta x)^2} \\
& [(\kappa_{+x})(T_{2,iy,iz} - T_{1,iy,iz}) \\
& - \left(\frac{\kappa_{BX,iy,iz}\kappa_{1,iy,iz}}{\kappa_{BX,iy,iz} + \kappa_{1,iy,iz}} \right) (T_{1,iy,iz} - T_{BX,iy,iz}) \\
& + (\kappa_{+y})(T_{1,iy+1,iz} - T_{1,iy,iz}) \\
& - (\kappa_{-y})(T_{1,iy,iz} - T_{ix,iy-1,iz}) \\
& + (\kappa_{+z})(T_{1,iy,iz+1} - T_{1,iy,iz}) \\
& - (\kappa_{-z})(T_{1,iy,iz} - T_{1,iy,iz-1})] \\
& - T_{1,iy,iz}\rho_{ix,iy,iz}C_{Vix,iy,iz} \left(\frac{1}{(2\delta t)} + \frac{\tau}{(\delta t)^2} \right).
\end{aligned} \tag{50}$$

The κ of the boundary interactions at the $x=1$ cells can be represented as

$$\frac{2\kappa_{BX,iy,iz}\kappa_{1,iy,iz}}{\kappa_{BX,iy,iz} + \kappa_{1,iy,iz}} = \kappa_{BX} \tag{51}$$

and interaction at the $x = NX$ cell as

$$\frac{2\kappa_{BNX,iy,iz}\kappa_{NX,iy,iz}}{\kappa_{BNX,iy,iz} + \kappa_{NX,iy,iz}} = \kappa_{BNX} \tag{52}$$

. The terms in the y and z axis are identical to the previous x-axis case so are omitted.

$$H(\kappa, \mathbf{r})T = \frac{1}{(\delta x)^2} [(\kappa_{+x})(T_{2,iy,iz} - T_{1,iy,iz}) - (\kappa_{BX})(T_{1,iy,iz} - T_{BX,iy,iz})] \quad (53)$$

This makes the boundary term much more transparent, for $ix = 1$, the boundary element must be

$$B_{1,iy,iz} = -\frac{1}{(\delta x)^2} [(\kappa_{BX})(T_{BX,iy,iz})] \quad (54)$$

For the opposite side, the result is (and it is symmetric)

$$B_{NX,iy,iz} = -\frac{1}{(\delta x)^2} [(\kappa_{BNX})(T_{BX,iy,iz})] \quad (55)$$

Thus for any boundary element an additive term. If iy and ix are 1 and or NX/NY then both the Y-boundary and x-boundary terms can be summed together, and the same method applies to the other dimensions and combinations of them.

Matrix form

The result is an equation in the form $H_{IJ}T_J = S_I$ which when expanded out for a $2 \times 2 \times 2$ system looks like,

$$\begin{pmatrix} \kappa & \kappa_{+x} & \kappa_{+y} & 0 & \kappa_{+z} & 0 & 0 & 0 \\ \kappa_{-x} & \kappa & 0 & \kappa_{+y} & 0 & \kappa_{+z} & 0 & 0 \\ \kappa_{-y} & 0 & \kappa & \kappa_{+x} & 0 & 0 & \kappa_{+z} & 0 \\ 0 & \kappa_{-y} & \kappa_{-x} & \kappa & 0 & 0 & 0 & \kappa_{+z} \\ \kappa_{-z} & 0 & 0 & 0 & \kappa & \kappa_{+x} & \kappa_{+y} & 0 \\ 0 & \kappa_{-z} & 0 & 0 & \kappa_{-x} & \kappa & 0 & \kappa_{+y} \\ 0 & 0 & \kappa_{-z} & 0 & \kappa_{-y} & 0 & \kappa & \kappa_{+x} \\ 0 & 0 & 0 & \kappa_{-z} & 0 & \kappa_{-y} & \kappa_{-x} & \kappa \end{pmatrix} \begin{pmatrix} T_{1,1,1} \\ T_{2,1,1} \\ T_{1,2,1} \\ T_{2,2,1} \\ T_{1,1,2} \\ T_{2,1,2} \\ T_{1,2,2} \\ T_{2,2,2} \end{pmatrix} = \begin{pmatrix} S_{1,1,1} \\ S_{2,1,1} \\ S_{1,2,1} \\ S_{2,2,1} \\ S_{1,1,2} \\ S_{2,1,2} \\ S_{1,2,2} \\ S_{2,2,2} \end{pmatrix}. \quad (56)$$

The form of the H-matrix is clearer with a slightly bigger system size ($5 \times 5 \times 5$) in Fig. 6.

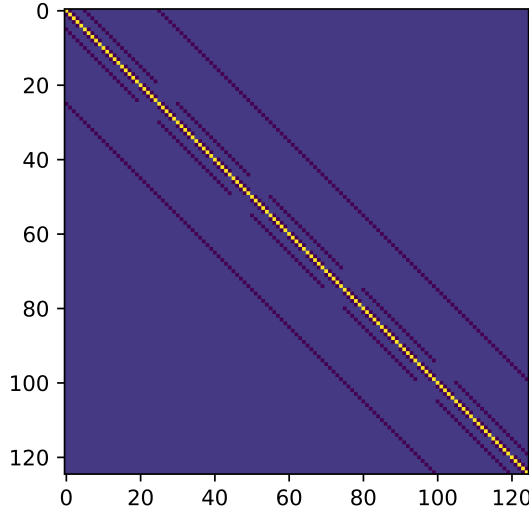


Figure 6: Showing the elements of the H-matrix, blue is 0 and represents no interaction, yellow is the self term, and purple is the interactions with the self term for the x,y,z axis.

κ at cell boundaries

There is an inherent issue in using the destination thermal conductivity for interaction terms, it is not spatially symmetric, leading to breaking time-reversal symmetry. For example, heat moving from cell A to B will use B's conductivity, and vice versa, B to A will use A but this leads to if you were to reverse the heat flow you would end up with a different amount of energy transfer if A and B are not equal. A mutual definition of thermal conductivity at the boundary is required to solve this issue. This can be highlighted by considering the steady state. To begin the heat transfer rate J as described by Fourier's law

$$J = -\kappa \nabla T, \quad (57)$$

where κ is the thermal conductivity, and ∇T is the temperature gradient.

The conservation of energy with the steady state condition requires that for two adjacent cells A and B the heat flux into A (q_{BA}) must be equal to the heat flux out of B (J_{AB}). This can be written

$$J_{AB} - J_{BA} = 0 \quad (58)$$

Substituting in the equation described by Fourier's law, it can be obtained:

$$J_{AB} = -\kappa_{AB} \nabla T \quad (59)$$

$$J_{BA} = -\kappa_{BA} \nabla T \quad (60)$$

where κ_{AB} and κ_{BA} are the thermal conductivity's for the heat transfer from A to B and B to A , respectively. It then follows that

$$-\kappa_{AB} \nabla T + \kappa_{BA} \nabla T = 0 \quad (61)$$

and therefore

$$\kappa_{AB} = \kappa_{BA} \quad (62)$$

where κ is a material property and should only depend on the material that is present. With this, it has been shown that coupled conductivity must be used to describe the interface conductivity at the boundary.

To determine an expression for the coupled conductivity the thermal resistance can be utilized, which is defined as

$$R = \frac{\Delta x}{A \kappa}, \quad (63)$$

where Δx is the path length, A is the conducting area and κ is the thermal conductivity.

In series, the total thermal resistance is the sum

$$R_{\text{total}} = R_1 + R_2 + R_3 + \dots \quad (64)$$

when considering thermal resistances it can be assumed that the discrete points of the mesh are space-filling. That is to say that for 2 adjacent cells A and B, half the distance from one to the next will have the physical properties of point A and the other half will have the physical properties of point B.

The next step is to approximate the heat flowing from the centre of cell A to the centre of cell B. The thermal resistance of each cell can be defined as

$$R_A = \frac{\frac{1}{2}\Delta x_A}{a \kappa_A} \quad (65)$$

$$R_B = \frac{\frac{1}{2}\Delta x_B}{a \kappa_B} \quad (66)$$

For two adjacent cells the area, a , must be the same for both. Now, by Eq. 64, simply add these terms to get the coupled thermal resistance.

$$R_{AB} = R_A + R_B \quad (67)$$

The coupled conductivity can be defined as,

$$\kappa_{AB} = \frac{\frac{1}{2}\Delta x_A + \frac{1}{2}\Delta x_B}{A R_{AB}} \quad (68)$$

which substituting in and simplifying gives

$$\kappa_{AB} = \frac{(\Delta x_A + \Delta x_B) \kappa_A \kappa_B}{\Delta x_B \kappa_A + \Delta x_A \kappa_B} \quad (69)$$

and in the case of a uniform grid, this becomes

$$\kappa_{AB} = \frac{2 \kappa_A \kappa_B}{\kappa_A + \kappa_B} \quad (70)$$

This is the harmonic average commonly used to approximate thermal contact resistance.

The computational method for solving this matrix equation to obtain the temperature distribution is discussed in Appendix B.

3 Micro scale (Material properties)

The kinetic theory of gases [8] states,

$$\kappa \propto C_V v^2 \tau, \quad (71)$$

where κ is the thermal conductivity, C_V is the specific heat capacity, v is the average phonon velocity, and τ is the average phonon relaxation time. Specific heat capacity, at constant volume (C_V), is defined as the change in internal energy due to a change in temperature at a constant volume,

$$C_V = \left. \frac{dU}{dT} \right|_V. \quad (72)$$

The internal energy can be written as a Taylor expansion about small displacements $u_{i,j}$ about the equilibrium ($\frac{dU}{dx} = 0$) as,

$$U = U_0 + \sum_i \frac{dU}{dx} u_i + \frac{1}{2} \sum_{i,j} \frac{d^2 U}{dx^2} u_i u_j + \frac{1}{3!} \sum_{i,j,k} \frac{d^3 U}{dx^3} u_i u_j u_k + \dots, \quad (73)$$

the second and higher-order terms are related to the phonon modes [25]. This relates the specific heat capacity directly to the phonon modes and distribution, by extension this means the thermal properties (κ & C_V) of a system can be determined by calculating phonon properties.

There are many methods for calculating phonons (depending on spatial and temporal scales), such as using Molecular dynamics (MD) [32], Density functional theory [33], Greens Function Method [34], Lattice Dynamics, and Boltzmann transport [35]. In this study, we will calculate the material's relative internal energy using Density Functional Theory to calculate the phonon modes.

3.1 Density Functional Theory

One way we can calculate phonons from first principles (using fundamental laws of physics i.e. quantum mechanics), is to start by calculating the ground state energy of a material (why is explained in the phonon section). This can also be done from first principles using Density Functional Theory (DFT).

DFT is a method used in theoretical physics for solving the many-body Schrodinger equation for a crystal. Solving the Schrodinger equation is done by re-postulating the many-body Schrodinger equation in terms of charge density [36].

The following steps are used to adjust the kinetic energy and potential terms of the many-body time-independent Schrodinger equation to a charge density form. The time-independent Schrodinger equation for electrons and ions in a system is,

$$\begin{aligned} & \left(\frac{-\hbar^2}{2} \sum_i^{N_{\text{ion}}} \frac{\nabla_i^2}{m_i} - \frac{\hbar^2}{2m_e} \sum_i^{N_{\text{electron}}} \nabla_i^2 + \sum_{i,j} V(R_1, \dots, R_m; r_1, \dots, r_n) \right) \psi(R_1, \dots, R_m; r_1, \dots, r_n) \\ &= E \psi(R_1, \dots, R_n; r_1, \dots, r_n). \end{aligned} \quad (74)$$

The first term refers to the kinetic energy of ions, the second term refers to the kinetic energy of the electrons, and the third term refers to the coulomb potential of ions and electrons interacting amongst themselves or with each other. R is the position of ions and r is the position of electrons. ψ is the combined eigenfunction of ions and electrons, and E is an eigenenergy of the system. m_e and m_i are the mass of an electron and the ions respectively.

To simplify, the Born Oppenheimer approximation is used to assume that the relative motion of electrons is effectively instantaneous relative to ionic motion. Using this to view the system at a time scale that the ions may be treated as stationary, the approximation for the kinetic energy of the ions is zero, the ion-to-electron potential can be treated as an external potential, and the ion-to-ion potential can be approximated as a static background effect. This leads to the assumption that the two eigenfunctions of the ions and electrons can be separated,

$$\psi(R_1, \dots, R_m; r_1, \dots, r_n) = \Phi(R_1, \dots, R_m) \phi(r_1, \dots, r_n). \quad (75)$$

This makes solving for the ions and the electrons independently solvable problems.

Next two Hohenberg-Kohn theorems are described. The first Hohenberg-Kohn theorem states that 'the ground state particle density of any system of interacting particles is determined uniquely by the external potential ($V_{\text{ext}}(\mathbf{r})$) acting on the system' [37]. The second Hohenberg-Kohn theorem states that 'for any external potential ($V_{\text{ext}}(\mathbf{r})$), the energy of the system is a universal function of the density $n(\mathbf{r})$; where the density that returns the global minimum value of this energy functional is the ground state density $n_0(\mathbf{r})$ ' [37]. Applying these theorems, the ground state electron density, $n_0(\mathbf{r})$, is approximated by using the background potential in which they sit (i.e. the background ion potential ($V_{\text{ext}}(\mathbf{r})$)) and is the unique solution to the system. From this unique solution, the energies related to the ground state electron density can be used to determine the ground state of the system as a whole.

The electron charge density is defined as,

$$n(\mathbf{r}) = Ne \int \phi^\dagger(\mathbf{r}_1 \dots \mathbf{r}_n) \phi(\mathbf{r}_1 \dots \mathbf{r}_n) d\mathbf{r}_1 \dots d\mathbf{r}_n \quad (76)$$

where \mathbf{r} is the positions, N is the number of electrons and e is the elementary charge. This is the probability distribution for electrons multiplied by N and e .

In general, it cannot be assumed that the charge density of the non-interacting particles is the same as the charge density of interacting particles. However, Kohn Sham proposed an approach utilizing a fictitious non-interacting system with a ground-state charge density equivalent to the interacting one. Kohn Sham's equation takes the form,

$$\left(-\frac{\hbar^2}{2m_e} \nabla^2 + V_s(\mathbf{r}) \right) \phi(\mathbf{r}) = \epsilon \phi(\mathbf{r}), \quad (77)$$

where the first term refers to the kinetic energy of the electrons, the second is a non-interaction potential, ϵ are the eigenvalues of the Kohn Sham electrons, and $\phi(\mathbf{r})$ is the wave function of

the Kohn Sham electrons.

The potential V_s is constructed as,

$$V_s(\mathbf{r}) = V_{\text{ext}}(\mathbf{r}) + \frac{e^2}{4\pi\epsilon_0} \int \frac{n(\mathbf{r}')}{|\mathbf{r} - \mathbf{r}'|} d^3\mathbf{r}' + V_{\text{XC}}, \quad (78)$$

where there is an external potential term ($V_{\text{ext}}(\mathbf{r})$) for the ion-electron interaction, the second term is a Hartree term which describes the electron-electron Coulomb repulsion. The final term is an exchange-correlation potential (V_{XC}) for the electron-electron interaction, see Eq. 78.

The process of solving this Kohn Sham equation using density functional theory calculation is as follows: Start by using an initial guess of charge density and solve the characteristic equation of the Kohn Sham equation, Eq. 77, to obtain eigenfunctions and eigenvalues. The eigenfunctions (wave function of Kohn Sham electrons) produce a charge density,

$$n(\mathbf{r}) = \sum_i |\phi_i(\mathbf{r})|^2, \quad (79)$$

this is compared to the initial guess, where n is the electron density and ϕ is the eigenfunctions of the Kohn Sham electrons. If the initial charge density does not equal the calculated charge density within the specified tolerance, use this result as the new charge density and repeat. The iteration stops when the input charge density and the calculated charge density converge. This output charge density is that of the structure's ground state energy. This is implementing the second Hohenberg-Kohn theorem as stated above.

Density functional theory is a popular tool enabling the study of material properties. With it, a wide range of systems can be investigated, including ion-intercalated systems' thermodynamic properties.

The benefits of theoretical analysis are shown in Fig. 7, where the results of density functional theory calculations are shown to closely match those of the experiment, with the largest discrepancy being only $\tilde{0.5}$ V for LiCoO₂ [38].

The advantages of density functional theory are that it has been shown to agree with experimental results to a high degree of accuracy (see Fig. 7). Using DFT we can relax the structure, allowing the atoms to move and not be fixed to their original positions to find the ground state atomic positions for the structure. This allows us to capture the ground state structure and its subsequent properties more accurately.

The disadvantages of density functional theory are that to have a higher accuracy final accuracy (a better convergence of the charge density) there is a much higher computational cost. Another disadvantage is the result of the intrinsic use of approximations, the electronic band gaps for the structure can be too small due to an underestimate of the coulomb repulsion. For our project, the level of accuracy is sufficient as shown in Fig. 7.

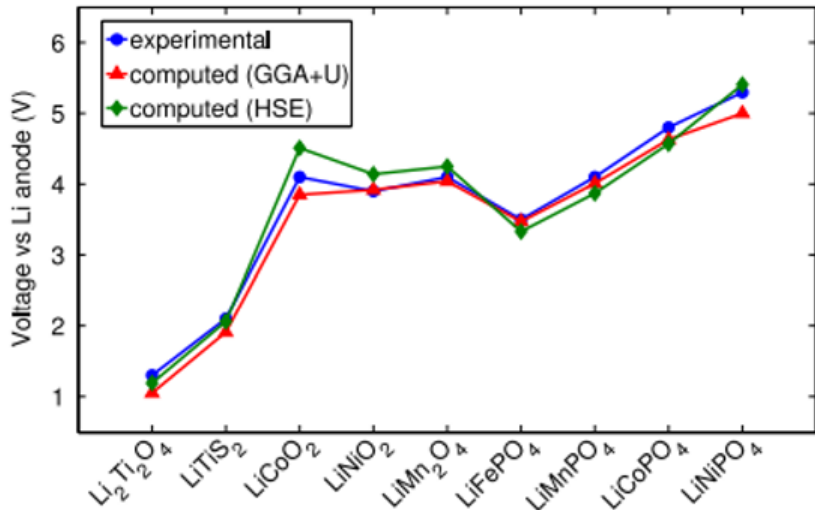


Figure 7: A comparison between voltages calculated using density functional theory (red and green) and experimental results (blue). GGA+U employs a potential (+U) term correcting for higher orbital electrons, whilst HSE employs a Hartree Fock correction[38].

3.2 Phonons

Phonon and thermal properties can be determined by utilizing a frozen phonon method for calculating the force constant matrix. This method is described in detail by Atsushi Togo [39]: The potential energy of a system can be expanded out in a Taylor series as,

$$V = \phi_0 + \sum_i \phi' u_i + \frac{1}{2} \sum_{i,j} \phi'' u_i u_j + \frac{1}{3!} \sum_{i,j,k} \phi''' u_i u_j u_k + \dots \\ = V_0 + V_1 + H_{\text{Harmonic}} + H_{\text{Anharmonic}} + \dots \quad (80)$$

where $\phi_0, \phi', \phi'', \phi''',$ are the 0th, 1st, 2nd, and 3rd order force constants respectively. Higher-order terms can be considered but have a larger computation demand. ϕ' is equal to 0 as we calculate the displacement u from equilibrium, and it would be the force the atoms experience at equilibrium which should be 0. ϕ_0 is set to 0 as it's just a potential shift and is frame of reference dependant. u_i, u_j, u_k are the i,j,k atoms displacements.

Harmonic approximation

For some thermal properties such as heat capacity at constant volume, only the harmonic term (2nd order force constant) is considered, Eq. 81, the anharmonic (3rd order term) and higher order terms are not.

$$\phi'' = \frac{\delta V}{\delta u_i \delta u_j} \quad (81)$$

The total energy of the system can be written as ($\bar{u} = \sqrt{m_i}u_i$, \bar{u} is mass normalized displacement):

$$H_{\text{Harm}} = \sum_i \frac{1}{2} \left(\frac{d\bar{u}_i}{dt} \right)^2 + \frac{1}{2} \sum_{i,j} \bar{u}_i \phi''_{i,j} \bar{u}_j \frac{1}{\sqrt{m_i m_j}} \quad (82)$$

The reduced force constant can be expressed as,

$$\bar{\phi}_{i,j}'' = \frac{1}{\sqrt{m_i m_j}} \phi_{i,j}. \quad (83)$$

$\bar{\phi}''$ can be diagonalized as,

$$\bar{\phi} = U \Omega^2 U^T \quad (84)$$

where $\Omega^2 = \text{diagonal}(\dots, \omega_n, \dots)$ and U is the orthogonal matrix whose columns are the eigenvectors $w_i(n)$ where n denotes the index of the normal modes. Therefore the eigenvector for this system can be expressed as,

$$\sum_j \bar{\phi}_{i,j} w_j = \omega^2 w_i. \quad (85)$$

Bloch theorem states that the wave function of a crystal that is the solution to the Schrodinger equation can be written as a product of a plane with a function with a periodicity equal to that of the crystal structure [40]. Using Bloch's theorem to re-express the eigenfunctions into,

$$w_i = \frac{1}{\sqrt{N}} W_i e^{i\mathbf{q} \cdot \mathbf{R}_i^0}, \quad (86)$$

the final solution for the phonon frequency eigenvalues, the phonon eigenfunctions and the dynamical matrix is,

$$\sum_j D_{i,j} W_j = \omega^2 W_i. \quad (87)$$

Furthermore, we can now re-express the atomic displacements as a function of the eigenfunctions of the phonons,

$$u_i = \frac{1}{\sqrt{N m_k}} \sum_{\mathbf{q}\nu} Q(\mathbf{q}\nu) W_i(\mathbf{q}\nu) e^{i\mathbf{q} \cdot \mathbf{R}_i^0}. \quad (88)$$

Q is an energy of phonon mode in terms of the annihilation and creation operators and is defined as,

$$Q(\mathbf{q}\nu) = \sqrt{\frac{\hbar}{2\omega_{\mathbf{q}\nu}}} (a_{\mathbf{q}\nu} + a_{-\mathbf{q}\nu}^\dagger) \quad (89)$$

with the dynamical matrix written in the form,

$$D_{i,j} = \sum_{i,j} \frac{e^{-i\mathbf{q} \cdot \mathbf{R}_i^0}}{\sqrt{N}} \bar{\phi}_{i,j} \frac{e^{i\mathbf{q} \cdot \mathbf{R}_j^0}}{\sqrt{N}} = \frac{1}{N \sqrt{m_i m_j}} \sum_{i,j} \bar{\phi}_{i,j} e^{i\mathbf{q} \cdot (\mathbf{R}_j^0 - \mathbf{R}_i^0)} = \frac{1}{\sqrt{m_i m_j}} \sum_j \bar{\phi}_{0i,j} e^{i\mathbf{q} \cdot (\mathbf{R}_j^0 - \mathbf{R}_0^0)}. \quad (90)$$

The heat capacity at constant volume, C_V , can be calculated as the above equations and is of the form:

$$C_{V,\text{Harm}} = \sum_{qv} k_B \left(\frac{\hbar\omega_{qv}}{k_B T} \right)^2 \frac{\exp\left(\frac{\hbar\omega_{qv}}{k_B T}\right)}{\exp\left(\frac{\hbar\omega_{qv}}{k_B T}\right) + 1} \quad (91)$$

The phonon group velocity is another useful value to be able to obtain, the equation for which is trivial:

$$v_{qs,\alpha} \equiv \frac{\delta\omega_{qv}}{\delta q_\alpha} \quad (92)$$

Anharmonic approximation

Thermal properties such as lattice thermal conductivity and scattering times require determining the 3rd-order force constants. The anharmonic term in Eq. 80 can be expressed in terms of phonon operators instead of atomic displacements,

$$H_{\text{Anharmonic}} = \sum_{\lambda,\lambda',\lambda''} \phi_{\lambda,\lambda',\lambda''} (a_\lambda + a_{-\lambda}^\dagger) (a_{\lambda'} + a_{-\lambda'}^\dagger) (a_{\lambda''} + a_{-\lambda''}^\dagger). \quad (93)$$

$\phi_{\lambda,\lambda',\lambda''}$ is obtained by substituting Eq. 88 & 89 into Eq. 80,

$$\begin{aligned} \phi_{\lambda,\lambda',\lambda''} = & \frac{1}{\sqrt{N}} \frac{1}{3!} \sum_{i,j,k} W_{\lambda,i} W_{\lambda',j} W_{\lambda'',k} \\ & \times \sqrt{\frac{\hbar}{2m_i\omega_\lambda}} \sqrt{\frac{\hbar}{2m_j\omega'_\lambda}} \sqrt{\frac{\hbar}{2m_k\omega''_\lambda}} \\ & \times \sum_{j,k} \phi_{0i,j,k} e^{i\mathbf{q}' \cdot (\mathbf{R}_j^0 - \mathbf{R}_{0i}^0)} e^{i\mathbf{q}'' \cdot (\mathbf{R}_k^0 - \mathbf{R}_{0i}^0)} \times \\ & e^{i(\mathbf{q} + \mathbf{q}' + \mathbf{q}'') \cdot \mathbf{R}_{0i}^0} \Delta(\mathbf{q} + \mathbf{q}' + \mathbf{q}''). \end{aligned} \quad (94)$$

The imaginary part of phonon self-energy $\Gamma_\lambda(\omega)$ is calculated using many body perturbation theory [41],

$$\begin{aligned} \Gamma_\lambda(\omega) = & \frac{18\pi}{\hbar^2} \sum_{\lambda'\lambda''} |\phi_{-\lambda\lambda'\lambda''}|^2 (n_{\lambda'} + n_{\lambda''} + 1) \\ & \times [\delta(\omega - \omega_{\lambda'} - \omega_{\lambda''}) - \delta(\omega + \omega_{\lambda'} + \omega_{\lambda''})] \\ & + (n_{\lambda'} + n_{\lambda''}) [\delta(\omega + \omega_{\lambda'} - \omega_{\lambda''}) - \delta(\omega - \omega_{\lambda'} + \omega_{\lambda''})], \end{aligned} \quad (95)$$

the phonon self energy is used to calculate the phonon lifetime. The phonon lifetime can be written in the form ($\omega_\lambda = \omega$),

$$\tau_\lambda = \frac{1}{2\Gamma_\lambda(\omega_\lambda)}. \quad (96)$$

Using Eq. 91, 96 & 92, the lattice thermal conductivity can be written as,

$$\kappa = \frac{1}{NV_c} \sum_\lambda C_\lambda \mathbf{v}_\lambda \otimes \mathbf{v}_\lambda \tau_\lambda \quad (97)$$

From the use of the 2nd-order harmonic and 3rd-order anharmonic potentials, it is possible to obtain the thermal properties of a material.

4 Results

4.1 ZrS₂

We first investigate the behaviour of lithiated ZrS₂. To demonstrate the effectiveness of our methodology, we compare our calculated voltage dependence with % Li intercalated with [16]. Our results, Fig. 8, show that the voltage (see Appendix D for calculation) of the system decreases with lithium intercalation, the voltage remains greater than 0 at Li₁ZrS₂ suggesting even more lithium could be intercalated. The results indicate that ZrS₂ is a cathode material in agreement with the results of [16].

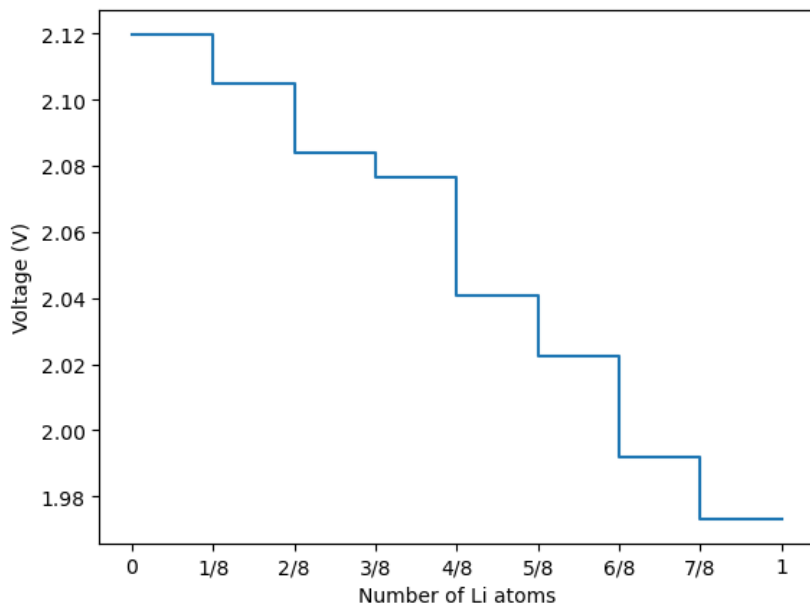


Figure 8: Voltage profile for Li_xZrS₂.

Then we investigate the heat capacity of Li_xZrS₂ which is shown in Fig. 9. We see that the material adopts 3D characteristics at both low and high levels of intercalation as the heat capacity $\approx T^3$. As expected, increasing the density increases the overall heat capacity per mol, due to the extra degree of freedom given.

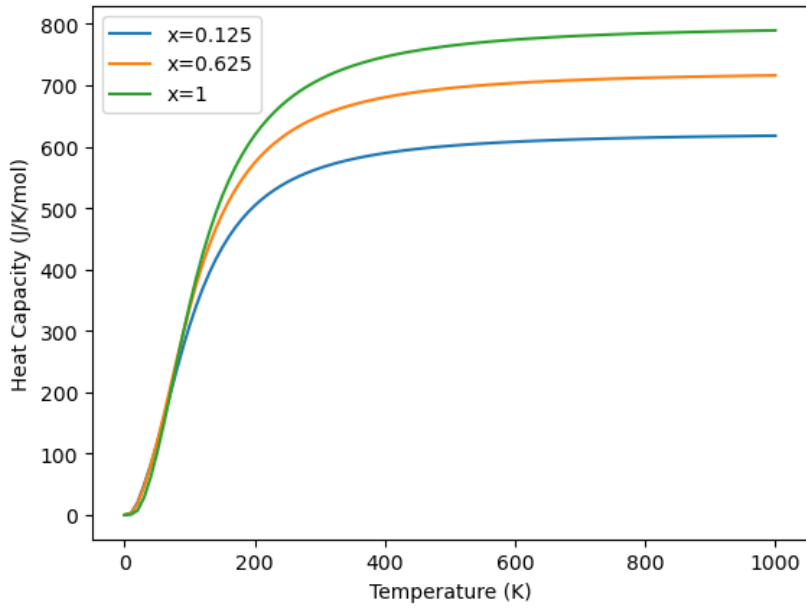


Figure 9: The heat capacity of Li_xZrS_2 for varying levels of intercalation (x).

To further investigate the thermal and phase stability properties of LiZrS_2 , we have calculated using our first principle methods the phonon dispersion relations of lithiated ZrS_2 at various intercalation levels. Fig. 11 shows the phonon dispersion relation for 0.125-1 lithium per ZrS_2 . Our results show that unusually for phonon modes, a large THz gap opens in the 4.40 to 5.65 THz range.

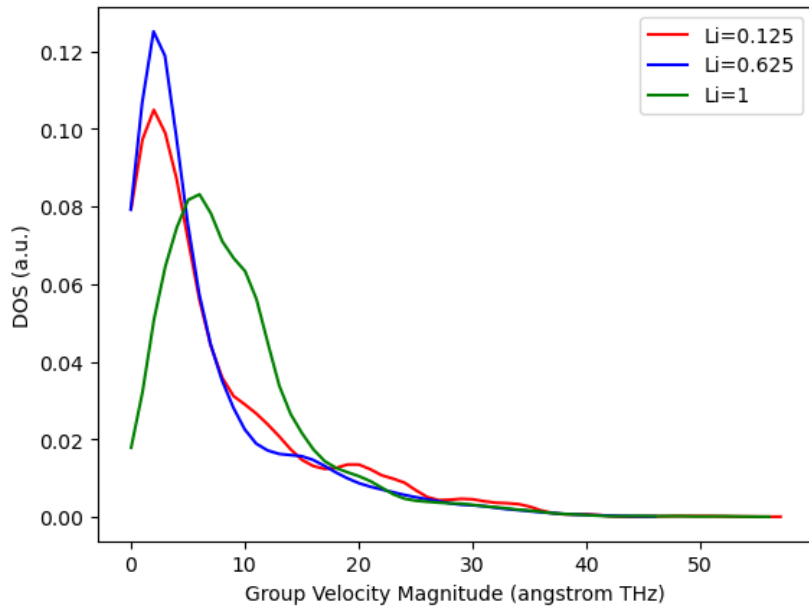
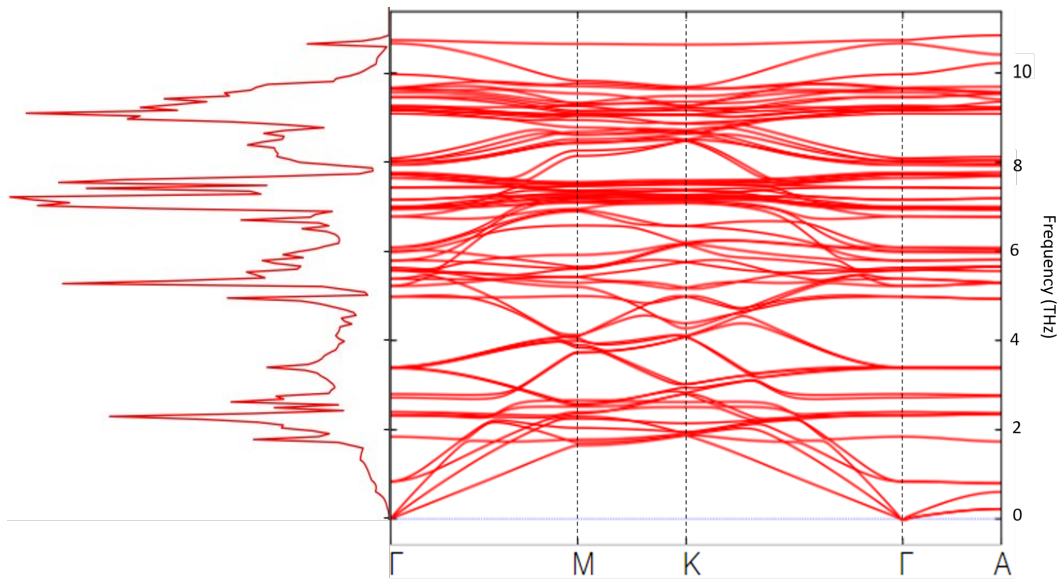
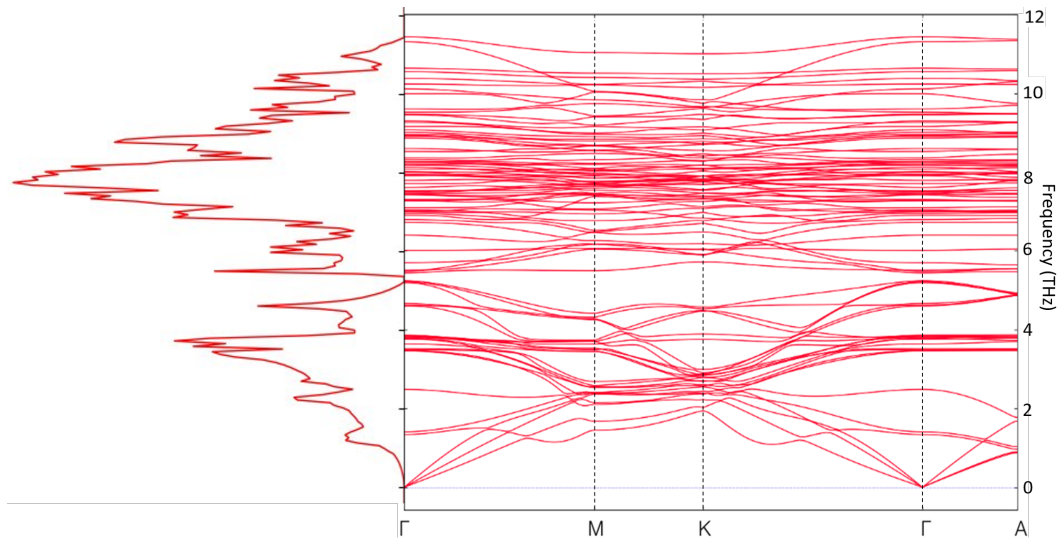


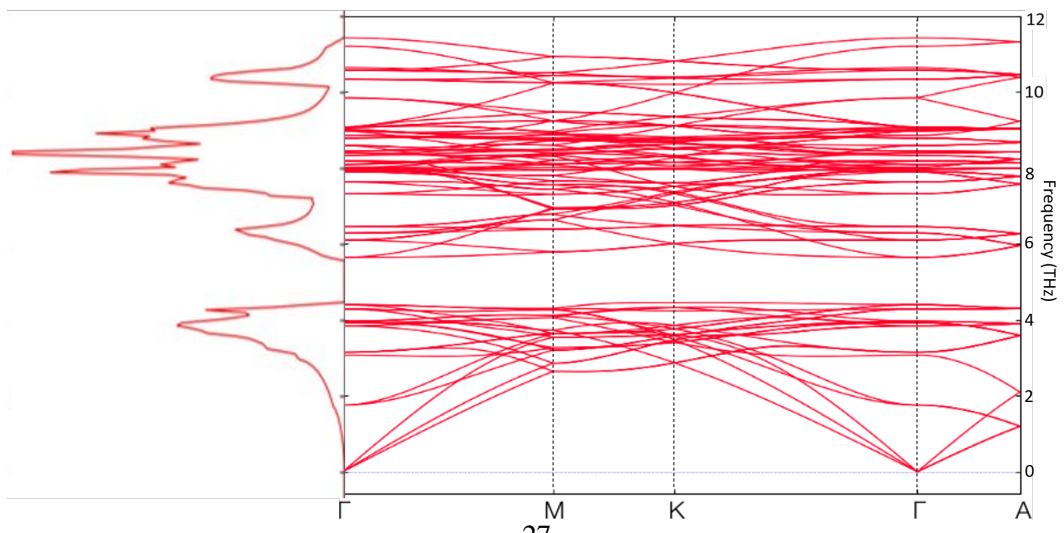
Figure 10: The density of states (% of modes with corresponding group velocity) of the phonon group velocity for the phonon dispersions, Fig. 11a, 11b, and 11c.



(a) The phonon dispersion relation (Frequency is in THz) for $\text{Li}_{0.125}\text{ZrS}_2$, the density of states of the modes on the left.



(b) The phonon dispersion relation (Frequency is in THz) for $\text{Li}_{0.625}\text{ZrS}_2$, the density of states of the modes on the left.



(c) The phonon dispersion relation (Frequency is in THz) for LiZrS_2 , the density of states of the modes on the left.

Figure 11

An unexpected result is the phononic band gap that appears as more lithium is put into the host structure. Figures Fig. 11a to Fig. 11c show the appearing phonon band gap opening up between 4 and 6 THz across all directions in the reciprocal space. There is a 61% increase in the group velocity of the lowest acoustic Γ to M branch for $Li = 0.125$ to $Li = 1$, Fig. 11a & 11c. Fig. 10 shows an initial decrease in average group velocity for $Li=0.625$ and $Li=0.125$ lithium intercalation, followed by an increase in the group velocity for $Li=1$. This increase in average group velocity (Fig. 10) corresponds to an increase in the thermal conductivity of the structure. This electrochemically controlled nano phononic crystal is an interesting phenomenon (see Appendix C on phononic crystals). Applications include Terahertz imaging and possibly thermoelectric.

4.2 Heat flow

Finally, when simulating the macroscale properties of a battery electrode, one could consider regions of high and low conductivity. A simple case is shown in Fig. 12 where every quadrant heats up differently, Fig. 14.



Figure 12: Schematic of simulated structure, all quadrants have the same properties apart from thermal conductivity. $Lo=1\text{Wm}^{-1}\text{K}^{-1}$, $Hi=100\text{W/m}^{-1}\text{K}^{-1}$, system starting temperature is 300K and the boundary thermal conductivity is 0 in the Z axis and $10\text{ Wm}^{-1}\text{K}^{-1}$ in all the other directions. The total system size is 0.1m by 0.1m by 0.1m with 30x30x1 cells in the X, Y, and Z directions respectively

Our results show that different quadrants of the electrode heat up significantly differently, Fig. 13. In Fig. 14 the variance in the average temperature of each quadrant is due to

different regions of high and low conductivity within the simulated electrode system. The asymmetry of the system results in different propagation of heat through each quadrant Fig. 12. Both lower thermal conductivity regions show a similar response to heating, they average a lower temperature than the top right quadrant but average relatively closer to each other than the high thermal conductivity quadrants. The higher thermal conductivity regions show a different result. The top right quadrant (high conductivity) that is touching the hot sources is significantly hotter than all the other quadrants, but the bottom left quadrant (high conductivity) remains on average cooler than all the other quadrants.

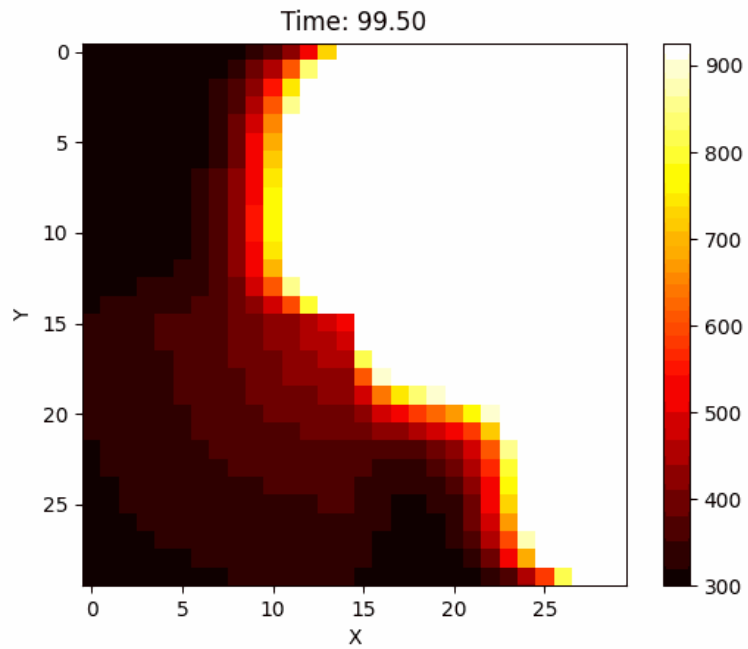


Figure 13: The heat map of the simulation of Fig. 12, the time is in seconds and the temperature bar is in kelvin.

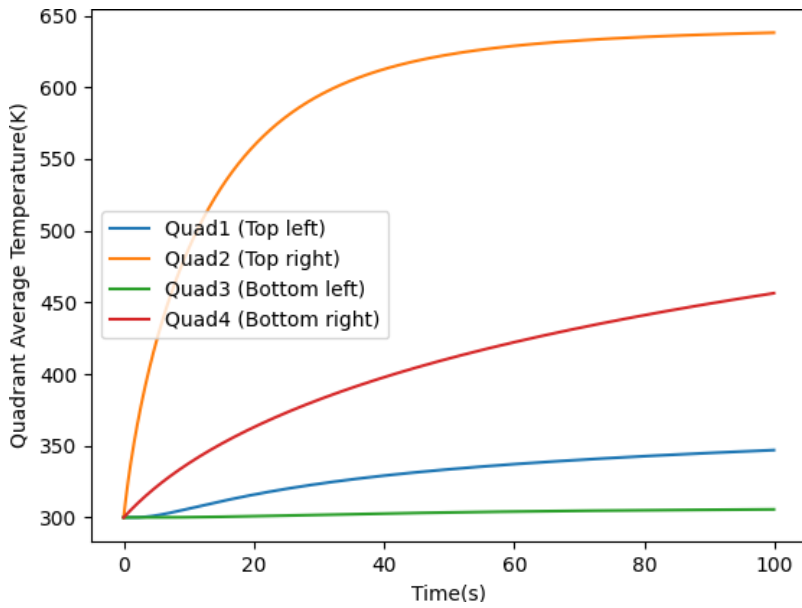


Figure 14: The average quadrant temperature over time for the simulation of the system in Fig. 12.

5 Conclusion

The investigation into the properties of Li_xZrS_2 reveals significant findings regarding its behaviour under various lithium intercalations (x). Our study focused on the thermal properties, phase stability, and phonon dispersion relations of Li_xZrS_2 at different intercalation levels. The results show a substantial THz gap in the phonon modes, specifically in the 4.40 to 5.65 THz range, which is unusual. This indicates unique properties that could be harnessed for advanced applications such as Terahertz imaging and thermoelectric materials. The next step is to calculate the thermal conductivity and investigate the phonon band gap further.

The study utilized the implicit finite difference method to solve the heat flow equations, transforming them into a matrix form suitable for computational modelling. This approach aimed to address the issues found in the finite element method, such as unphysical negative temperature regions and poor non-steady-state simulation performance. The results of the Heat Flow simulation show the necessity of simulated electrodes with time dynamic and spatially variant systems. The results show that the geometry of the electrode is an important factor when it comes to managing potential hot spots in the electrode, which can result in a breakdown. The Heat Flow model is in the development stage and is being used to model systems. Currently, it is being used to investigate the Cattaneo correction and the viability of measuring it in experiments.

Overall, even at this stage, both areas of the project are heading towards the goal of being able to model dynamic heat flow on a multi-scale level.

6 Appendix

6.1 Appendix A: Derivation from telegraphs equation

The Telegraphers equation, which describes voltage and current in transmission lines, can be analogously applied to heat transport, allowing us to model thermal conductivity with finite propagation speed. It has the form,

$$\frac{\delta^2 V}{\delta x^2} = LC \frac{\delta^2 V}{\delta t^2} + (RC + GL) \frac{\delta V}{\delta t} + GRV, \quad (98)$$

Where all letters have their usual electrical meaning and with the assumption V is a function of x and t . This equation can be described in a more general way,

$$\frac{\delta^2 V}{\delta x^2} = \frac{1}{v^2} \frac{\delta^2 V}{\delta t^2} + \frac{1}{\tau} \frac{\delta V}{\delta t}, \quad (99)$$

where v is the velocity and τ is the scattering/decay time. The next step is to transform this general equation into one that describes a particle ((q)s) field (n_{qs} , is the particle distribution function),

$$v_{qs}^2 \frac{\delta^2 n_{qs}}{\delta x^2} = \frac{\delta^2 n_{qs}}{\delta t^2} + \frac{1}{\tau_{qs}} \frac{\delta n_{qs}}{\delta t} \quad (100)$$

. It can be stated that all particles obey this equation and travel with a finite decay rate. Multiply through by $\tau_{qs} \hbar \omega_{qs}$, where symbols have usual meaning. This gives us,

$$v_{qs}^2 \tau_{qs} \frac{\delta^2 n_{qs} \hbar \omega_{qs}}{\delta x^2} = \tau_{qs} \frac{\delta^2 n_{qs} \hbar \omega_{qs}}{\delta t^2} + \frac{\delta n_{qs} \hbar \omega_{qs}}{\delta t} \quad (101)$$

. This gives a way to transform from particle distribution to T (where $K_B T = \sum_{qs} n_{qs} \hbar \omega_{qs}$). Taking the sum of this for all particles, the result can be rewritten as

$$v^2 \tau \frac{\delta^2 T}{\delta x^2} = \tau \frac{\delta^2 T}{\delta t^2} + \frac{\delta T}{\delta t}. \quad (102)$$

Also assuming that v_{qs} and τ_{qs} can be equal to the average of the values for all particles ($v_{qs} \approx v$ and $\tau_{qs} \approx \tau$). Finally, knowing conductivity takes the form $\kappa = \rho C_V v^2 \tau$, and multiplying through by ρC_V , the Cattaneo equation for a uniform system can be arrived at as:

$$\kappa \frac{\delta^2 T}{\delta x^2} = \tau \rho C_V \frac{\delta^2 T}{\delta t^2} + \rho C_V \frac{\delta T}{\delta t} \quad (103)$$

6.2 Appendix B: Solving the Thermal model

Sparse matrix storage

Compressed Sparse Row (CSR) Format

The Compressed Sparse Row (CSR) format is a way to store sparse matrices efficiently. In CSR format, the matrix is stored using three arrays: values, row pointers, and column indices. [42]

- **Values Array (values)**: This array contains the non-zero elements of the matrix in row-major order. For example, if the i th row of the matrix contains m non-zero elements, then the values of these elements are stored consecutively in the values array.
- **Row Pointers Array (row_ptr)**: This array contains $(n + 1)$ elements, where n is the number of rows in the matrix. The i th element of the row pointers array indicates the starting position of the i th row in the values array.
- **Column Indices Array (col_indices)**: This array contains the column indices of the non-zero elements in the values array. Each element in this array corresponds to the column index of the corresponding non-zero element in the values array.

Example

Consider the following (3×3) sparse matrix:

$$A = \begin{bmatrix} 1 & 0 & 0 \\ 0 & 0 & 2 \\ 3 & 0 & 4 \end{bmatrix}$$

In CSR format, this matrix would be represented as follows:

$$\text{values} = \begin{bmatrix} 1 & 2 & 3 & 4 \end{bmatrix}$$

$$\text{row_ptr} = \begin{bmatrix} 0 & 1 & 2 & 2 \end{bmatrix}$$

$$\text{col_indices} = \begin{bmatrix} 0 & 2 & 0 & 2 \end{bmatrix}$$

Here, the values array contains the non-zero elements of the matrix in row-major order, the row pointers array indicates the starting position of each row in the values array, and the column indices array contains the column indices of the non-zero elements.

Conjugate Gradient Method for Sparse Linear Systems

Overview

The Conjugate Gradient (CG) method is an iterative technique for solving linear systems of equations like the one we have formed for heat flow simulation ($Ax = b$). The method is as follows [43]:

1. **Initialization:** Start with an initial guess for the solution vector x_0 . The thermal model initial system temperature plus the difference in the two past time steps.
2. **Residual Calculation:** Calculate the residual vector $r_0 = b - Ax_0$, where A is the transformation matrix and b is the known solution.
3. **Conjugate Directions:** Choose a set of conjugate search directions $p(0), p(1), \dots, p(n-1)$, where n is the size of the system. For a symmetric matrix A , vectors $p(0), p(1), \dots, p(n-1)$ are said to be mutually conjugate with respect to A if:

$$p(i)^T A p(j) = 0 \quad \text{for } i \neq j \quad (104)$$

Our initial value of p is set equal to the initial residual vector. The congruence of p is crucial in the Conjugate Gradient method because it ensures that each search direction explores a different direction in the solution space, which helps accelerate convergence.

4. **Step size:** The coefficient α_k puts a limit on how much our solution changes in each iteration to help prevent overshooting the minimum ($x_{k+1} = x_k + \alpha_k p_{k+1}$). α_k is calculated as,

$$\alpha_k = \frac{p_{k+1}^T r_k}{p_{k+1}^T A p_{k+1}}. \quad (105)$$

5. **β coefficient** In addition to α_k , β_k is also used which serves a similar function as to change the search direction $p_{k+1} = r_{k+1} + \beta_k p_k$. The coefficient β_k is chosen in each iteration to ensure that the new search direction remains conjugate to the previous ones for the matrix (A). This ensures that the CG method converges efficiently. β_k can be calculated as,

$$\beta_k = \frac{r_{k+1}^T r_{k+1}}{r_k^T r_k}. \quad (106)$$

To understand conjugacy with respect to (A), consider two vectors (v_1) and (v_2). They are said to be conjugate for (A) if their inner product ($v_1^T A v_2$) is zero. In the CG method, the aim is to maintain conjugacy between successive search directions (p_k) and (p_{k+1}) concerning (A). This property helps the CG method converge faster.

6. **Iteration:** For each iteration $k \rightarrow k + 1$:

- Compute the next approximation of the solution: $x_{k+1} = x_k + \alpha_k p_k$

- Update the residual: $r_{k+1} = r_k - \alpha_k A p_k$.
 - Update the search direction: $p_{k+1} = r_{k+1} + \beta_k p_k$.
 - Update α_k and β_k .
 - Repeat
7. **Stopping Criterion:** Repeat the iteration until the residual becomes sufficiently small or a maximum number of iterations is reached.
8. **Solution:** Once converged, the current approximation x_k is the solution to the system $Ax = b$ or in our case $HT = S$.

Code state

The coded model can produce expected results for steady state and Fourier systems and is time-step independent.

Expected results are also produced for uniform and non-uniform system structures with heated boundaries. We have a fully working model that has a spatial resolution independent of cell heating.

Some investigation into the Cattaneo correction in particular how the frequency of a heated source and the value of τ affect the resultant temperature distribution concerning the Fourier result.

In addition, some experimental results for systems we can model to compare against are needed to fully test the model.

6.3 Appendix C: Additional Theory

Rattlers

An explanation for why ions intercalating into the electrodes cause a thermal conductivity change is when there are few ions intercalated into the structure they can act like phonon rattlers.

Phonon rattlers are loosely bound atoms or atoms within a crystal lattice exhibiting large amplitude vibrations. When a loosely bonded atom is added to a structure in regions of vacuum it can introduce new anharmonic bands into the band structure of the system. This new band adds acoustic scattering modes which reduces the thermal conductivity [44]. Adding more of these atoms into the structure may not yield the expected result, as they can cluster together, changing the phonon modes.

The clustering of the rattlers could reduce the effects of the rattling as they could form strong bonds together. Consequently, the weak bonding to the host material could become insignificant.

Phononic Crystals

Initial investigation in the project has shown phonon band gap behaviour in LiZrS₂, this is another mechanism that typically reduces thermal conductivity (like rattlers) which will also be investigated.

Phononic crystals represent a class of materials typically engineered with precision to exhibit a periodic arrangement at the micro- or nano-scales [45]. These materials possess a band gap within the phonon dispersion relation. This band gap acts as a forbidden zone for certain phonon frequencies, effectively impeding their propagation through the material.

This manipulation of phononic behaviour holds immense promise for tailoring thermal conductivity properties [25]. The manipulation of the phonon band gap has interesting applications such as for thermoelectrics and Terahertz imaging.

6.4 Appendix D: Voltages

Voltages for a material from DFT energies are calculated from,

$$V = \frac{E(\text{Li}_{a_2}\text{ZrS}_2) - (E(\text{Li}_{a_1}\text{ZrS}_2) + (a_2 - a_1)E(\text{Li}))}{(a_2 - a_1) \times -e}, \quad (107)$$

where $E(\text{Li}_a\text{ZrS}_2)$ is the energy of Li_aZrS_2 , $a_2 > a_1$, $E(\text{Li})$ is the energy of isolated/bulk Li, and e is elementary charge.

7 Code

Code is available on Github via <https://git.exeter.ac.uk/hepplestone/heatflow-mk2>

8 Acknowledgements

I acknowledge the use of Github Copilot to:

- generate code/code snippets (predictive coding) that I have adapted to include within my final assessment.

Copilot auto prompts so the initial inputs are not available. I acknowledge the use of Grammarly to:

- refine writing / improve grammar within my final assessment.

As Grammarly is being used throughout the writing process, keeping a version history of every change and then keeping track of the changes no longer incorporated is impractical and so not stored.

I acknowledge the use of Chatgpt, but not for writing and I'm happy to show how I use Chatgpt in my research.

References

- [1] M.R. Jongerden and B.R. Haverkort. Which battery model to use? *IET Software*, 3(6):445, 2009.
- [2] Noriko Kawakami and Yukihisa Iijima. Overview of battery energy storage systems for stabilization of renewable energy in japan. In *2012 International Conference on Renewable Energy Research and Applications (ICRERA)*, pages 1–5, 2012.
- [3] Ona Egbue and Suzanna Long. Barriers to widespread adoption of electric vehicles: An analysis of consumer attitudes and perceptions. *Energy Policy*, 48:717–729, September 2012.
- [4] Gary L. Brase. What would it take to get you into an electric car? consumer perceptions and decision making about electric vehicles. *The Journal of Psychology*, 153(2):214–236, September 2018.
- [5] Nikolaos Wassiliadis, Jakob Schneider, Alexander Frank, Leo Wildfeuer, Xue Lin, Andreas Jossen, and Markus Lienkamp. Review of fast charging strategies for lithium-ion battery systems and their applicability for battery electric vehicles. *Journal of Energy Storage*, 44:103306, December 2021.
- [6] Suji Kim, You Jin Kim, and Won-Hee Ryu. Zirconium disulfides as an electrode material alternative for li-ion batteries. *Applied Surface Science*, 547, May 2021.
- [7] Alison Lennon, Yu Jiang, Charles Hall, Derwin Lau, Ning Song, Patrick Burr, Clare P. Grey, and Kent J. Griffith. High-rate lithium ion energy storage to facilitate increased penetration of photovoltaic systems in electricity grids. *MRS Energy & Sustainability*, 6(1), June 2019.
- [8] Charles Kittel. *Introduction to Solid State Physics 8th Edition*. John Wiley & Sons, Inc, 2005.
- [9] Karl W. Boer & Udo W. Pohl. *Semiconductor Physics*. Springer Nature, 2018.
- [10] Xinghui Zhang, Zhao Li, Lingai Luo, Yilin Fan, and Zhengyu Du. A review on thermal management of lithium-ion batteries for electric vehicles. *Energy*, 238:121652, January 2022.
- [11] Can-Yong Jhu, Yih-Wen Wang, Chi-Min Shu, Jian-Chuang Chang, and Hung-Chun Wu. Thermal explosion hazards on 18650 lithium ion batteries with a vsp2 adiabatic calorimeter. *Journal of Hazardous Materials*, 192(1), 2011.

- [12] Gaohua Zhu, Jun Liu, Qiye Zheng, Ruigang Zhang, Dongyao Li, Debasish Banerjee, and David G. Cahill. Tuning thermal conductivity in molybdenum disulfide by electrochemical intercalation. *Nature Communications*, 7(1), October 2016.
- [13] Puqing Jiang, Xin Qian, and Ronggui Yang. Tutorial: Time-domain thermoreflectance (tdtr) for thermal property characterization of bulk and thin film materials. *Journal of Applied Physics*, 124(16), October 2018.
- [14] Naoki Nitta, Feixiang Wu, Jung Tae Lee, and Gleb Yushin. Li-ion battery materials: present and future. *Materials Today*, 18(5):252–264, June 2015.
- [15] M. S. Whittingham. Electrical energy storage and intercalation chemistry. *Science*, 192(4244):1126–1127, June 1976.
- [16] Conor Jason Price, Edward Allery David Baker, and Steven Paul Hepplestone. First principles study of layered transition metal dichalcogenides for use as electrodes in li-ion and mg-ion batteries. *Journal of Materials Chemistry A*, 11(23):12354–12372, 2023.
- [17] Mohammad Bagher Askari, Parisa Salarizadeh, Payam Veisi, Elham Samiei, Homa Saeidfirozeh, Mohammad Taghi Tourchi Moghadam, and Antonio Di Bartolomeo. Transition-metal dichalcogenides in electrochemical batteries and solar cells. *Micromachines*, 14(3):691, March 2023.
- [18] Pushpendra Kumar, Hatem Abuhimd, Wandi Wahyudi, Mengliu Li, Jun Ming, and Lain-Jong Li. Review—two-dimensional layered materials for energy storage applications. *ECS Journal of Solid State Science and Technology*, 5(11):Q3021–Q3025, 2016.
- [19] Naoki Nitta, Feixiang Wu, Jung Tae Lee, and Gleb Yushin. Li-ion battery materials: present and future. *Materials Today*, 18(5):252–264, June 2015.
- [20] Yanfeng Dong, Haodong Shi, and Zhong-Shuai Wu. Recent advances and promise of mxene-based nanostructures for high-performance metal ion batteries. *Advanced Functional Materials*, 30(47), April 2020.
- [21] A. A. Yaroshevsky. Abundances of chemical elements in the earth's crust. *Geochemistry International*, 44(1):48–55, January 2006.
- [22] Shafiq Ur Rehman, Abdus Samad, Muhammad Saeed, Bin Amin, Muhammad Hafeez, Irshad A. Mir, and ling Zhu. Computational insight of zrs2/graphene heterobilayer as an efficient anode material. *Applied Surface Science*, 551:149304, June 2021.
- [23] K. M. Abraham. How comparable are sodium-ion batteries to lithium-ion counterparts? *ACS Energy Letters*, 5(11), October 2020.

- [24] Y.M. Ali and L.C. Zhang. Relativistic heat conduction. *International Journal of Heat and Mass Transfer*, 48(12):2397–2406, 2005.
- [25] A. H. Harker. The physics of phonons, 2nd edition , by gyaneshwar p. srivastava. *Contemporary Physics*, 63(4), October 2022.
- [26] C. Cattaneo, J.K. de Fériet, and Académie des sciences (France). *Sur une forme de l'équation de la chaleur éliminant le paradoxe d'une propagation instantanée*. Comptes rendus hebdomadaires des séances de l'Académie des sciences. Gauthier-Villars, 1958.
- [27] James Clerk Maxwell. On the dynamical theory of gases. *Philosophical Transactions of the Royal Society of London*, 157:49–88, December 1867.
- [28] Stevan M. Cvetićanin, Dušan Zorica, and Milan R. Rapaić. Generalized time-fractional telegrapher's equation in transmission line modeling. *Nonlinear Dynamics*, 88(2), January 2017.
- [29] A.J. van der Merwe, N.F.J. van Rensburg, and R.H. Sieberhagen. Comparing the dual phase lag, cattaneo-vernotte and fourier heat conduction models using modal analysis. *Applied Mathematics and Computation*, 396, May 2021.
- [30] Á. Rieth, R. Kovács, and T. Fülöp. Implicit numerical schemes for generalized heat conduction equations. *International Journal of Heat and Mass Transfer*, 126:1177–1182, November 2018.
- [31] John Crank. *The mathematics of diffusion*. Oxford university press, 1979.
- [32] Ling Ti Kong. Phonon dispersion measured directly from molecular dynamics simulations. *Computer Physics Communications*, 182(10):2201–2207, October 2011.
- [33] L. Lindsay, C. Hua, X.L. Ruan, and S. Lee. Survey of ab initio phonon thermal transport. *Materials Today Physics*, 7:106–120, December 2018.
- [34] W. Zhang, T. S. Fisher, and N. Mingo. The atomistic green's function method: An efficient simulation approach for nanoscale phonon transport. *Numerical Heat Transfer, Part B: Fundamentals*, 51(4):333–349, March 2007.
- [35] Francis VanGessel, Jie Peng, and Peter W. Chung. A review of computational phononics: the bulk, interfaces, and surfaces. *Journal of Materials Science*, 53(8):5641–5683, October 2017.
- [36] Kyle A. Baseden and Jesse W. Tye. Introduction to density functional theory: Calculations by hand on the helium atom. *Journal of Chemical Education*, 91(12), November 2014.
- [37] C.C.M. Rindt and S.V. Gaastra-Nedea. Modeling thermochemical reactions in thermal energy storage systems. 2015.

- [38] V. L. Chevrier, S. P. Ong, R. Armiento, M. K. Y. Chan, and G. Ceder. Hybrid density functional calculations of redox potentials and formation energies of transition metal compounds. *Physical Review B*, 82(7), August 2010.
- [39] Atsushi Togo. First-principles phonon calculations with phonopy and phono3py. *Journal of the Physical Society of Japan*, 92(1), January 2023.
- [40] R.J. Martín-Palma J.M. Martínez-Duart and F. Agulló-Rueda. *Nanotechnology for Microelectronics and Optoelectronics*. Elsevier, 2006.
- [41] H. Bruus and K. Flensberg. *Introduction to Many-body quantum theory in condensed matter physics*. Oxford University Press, 2004.
- [42] Mahdi Soltan Mohammadi, Kazem Cheshmi, Ganesh Gopalakrishnan, Mary Hall, MM Dehnavi, Anand Venkat, Tomofumi Yuki, and Michelle Strout. Sparse matrix code dependence analysis simplification at compile time. 07 2018.
- [43] Magnus R. Hestenes and Eduard Stiefel. Methods of conjugate gradients for solving linear systems. *Journal of research of the National Bureau of Standards*, 49, 1952.
- [44] Mogens Christensen, Asger B. Abrahamsen, Niels B. Christensen, Fanni Juranyi, Niels H. Andersen, Kim Lefmann, Jakob Andreasson, Christian R. H. Bahl, and Bo B. Iversen. Avoided crossing of rattler modes in thermoelectric materials. *Nature Materials*, 7(10), August 2008.
- [45] Masahiro Nomura, Roman Anufriev, Zhongwei Zhang, Jeremie Maire, Yangyu Guo, Ryoto Yanagisawa, and Sebastian Volz. Review of thermal transport in phononic crystals. *Materials Today Physics*, 22, January 2022.